



# Evaluating the localised through-thickness load transfer and damage initiation in a composite joint using digital image correlation



G. Crammond, S.W. Boyd, J.M. Dulieu-Barton \*

University of Southampton, Engineering Sciences, Southampton, SO17 1BJ, UK

## ARTICLE INFO

### Article history:

Received 27 March 2013

Received in revised form 20 February 2014

Accepted 2 March 2014

Available online 12 March 2014

### Keywords:

B. Adhesion

B. Stress concentration

D. Mechanical testing

D. Non-destructive testing

E. Joint/Joining

## ABSTRACT

Experimental analysis of the stresses and strains in a glass fibre polymer composite double butt strap joint using digital image correlation (DIC) is described in the paper. Initially the strain fields through the thickness of the joint are derived from DIC measurements, capturing the effect of the initiation and development of cracks in the joint up to failure. It is demonstrated that the relatively small strains developed in the through-thickness direction are critical in the development of damage in the joint at the geometric discontinuity between the adherends. An experimental methodology is established to perform DIC at the mesoscopic scale, enabling accurate, high spatial resolution analysis of the small through-thickness strains around the discontinuity. The DIC enables the strains to be evaluated, their development monitored and hence establish their contribution to the failure process. To determine the full-field stresses in the joint experimentally derived materials properties are used. From component stress maps principal stresses maps are derived, which clearly show where the damage is initiating and its subsequent growth in the composite adherends until final failure of the joint.

© 2014 Elsevier Ltd. All rights reserved.

## 1. Introduction

Composite materials are being increasingly used in large scale high performance structural applications such as aircraft wings, wind turbine blades and marine structures. All of these structures experience high through-thickness loading due to in-service bending and torsional loads. The size of these composite structures requires that they are assembled from a number of smaller components, commonly utilising secondary structure such as stiffeners and strengthening ribs to achieve the necessary structural integrity. These components must be joined together using mechanical fasteners such as rivets and bolts, or using adhesive bonding. The latter offers lower weight assemblies, with fewer parts and reduced assembly time in comparison to the mechanical solutions [1,2].

The discontinuous nature of mechanically fastened and adhesively bonded joints necessitates through-thickness load transfer between components. In a mechanically fastened assembly, load is transferred between components across the bearing surfaces of the fastener. The fastener also provides through-thickness strength and reinforcement, generating local clamping forces which hold the component faces together. Load transfer in adhesively bonded

assemblies is facilitated by the chemical bond of the adhesive to the component surface. Therefore the load transfer across the discontinuity between components is heavily reliant upon the peel and shear strength of the adhesive, in addition to the through-thickness mechanical properties of the laminate [3].

Composite materials are strong in the in plane fibre direction, but are weak normal to the plane of the laminate, with the strength dominated by the mechanical properties of the brittle polymer matrix [4]. The weak through-thickness properties, and the relatively high through-thickness loading across the discontinuity in a bonded joint, makes composite adherends susceptible to the initiation of interlaminar cracks, which lead to failure of the joint. Improving the understanding of the through-thickness behaviour within the joint provides a means to better describe the load transfer and damage initiation mechanisms, enabling the development of more efficient composite structural joint designs and more accurate modelling approaches.

Research on adhesive joints has primarily assessed performance based upon ultimate tensile strength [5,6], and investigated improvements in strength through parametric geometry changes [7–9]. A limited number of studies, identified below, have experimentally analysed the stress and strain distributions developed within adhesive joints, or assessed how the observed features interact and contribute towards the damage mechanisms within the structure. Digital image correlation (DIC) has been used to

\* Corresponding author.

E-mail address: [janice@soton.ac.uk](mailto:janice@soton.ac.uk) (J.M. Dulieu-Barton).

analyse the contributions of axial, peel and shear strain at the adhesive interface between components in single lap joints [10], double butt strap joints (DBSJ) [11–13], and bonded repair patches [14]. Moiré interferometry has also been used to analyse the distribution and evolution of the shear and through-thickness strains within composite single lap joints [15], which identified that the material at the interface with the adhesive was subjected to large strains. High magnification Moiré interferometry has also been used to image small regions of interest around the discontinuity between adherends [16]. The high magnification increases the spatial resolution of the data and enabled observation of localised peel and shear concentrations which were not visible at lower magnification levels.

The work presented in the present paper builds upon previous analyses conducted by Boyd et al. [17,18], who investigated the stress distribution in glass fibre polymer composite double butt strap joints using thermoelastic stress analysis (TSA) [19]. A comparison of the TSA data was taken from a position of 20 mm away from the discontinuity in the joint with a 2D plane element finite element numerical model showing good agreement. However the stress metric generated from the TSA is a function of the sum of the principal stresses, so the individual components of stress cannot be separated without recourse to other data. Whilst TSA is useful as a tool for validation of models as demonstrated in [18], a function of the stress sum cannot be linked to any failure criterion. To achieve this, an experimental approach is required which can deliver the individual components of stress or strain from the joint as it fails.

In the paper DIC is used to evaluate the individual strain components generated in a DBSJ up to failure. The strain fields across the thickness of the joint are examined at increasing levels of magnification, providing high resolution measurement of the developing strains. Particular attention is given to the behaviour in the through-thickness direction, which has a significant influence on the initiation of damage within the composite structure. Experimental challenges related to conducting DIC at high magnification are overcome, and the strain fields that cause damage initiation and growth are captured with a high degree of confidence. Principal stresses around the discontinuity are obtained from measured material properties and manipulation of the strain data, which provides the localised material behaviour around the geometric discontinuity during the formation of damage.

## 2. Joint structure

The DBSJ configuration, shown in Fig. 1a and similar to that used by Boyd et al. [17], was selected for analysis. The symmetry of the joint geometry minimises specimen rotation under loading. This makes the specimen type an ideal starting point for DIC studies as compensating for large rigid body rotations introduces an added complication when attempting to use DIC on high magnification images. The DBSJ was constructed from 800 g/m<sup>2</sup> unidirectional and 450 g/m<sup>2</sup> chopped strand mat (CSM) glass fibre in a [CSM<sub>3</sub> O<sub>4</sub> CSM<sub>2</sub>]<sub>s</sub> layup. The resin infusion process was used to manufacture the laminate using Gurit Prime 20 LV epoxy resin. The layup created a 7.3 mm thick laminate with thick layers of dissimilar material as shown in Fig. 1b. The DBSJ was constructed with a width of 25 mm and an outer adherend overlap length of 25 mm. The inner adherends were 150 mm long separated by a 2 mm gap at the butt between the adherends. Araldite 2015, a two-part toughened structural epoxy adhesive, was used to bond the adherends together. The 0.6 mm adhesive bond line thickness was measured using optical microscopy.

Although the DBSJ does not represent a typical in-service joint configuration, it provides a demonstrator to show the capabilities

of DIC in evaluating the mechanical behaviour of complex composite structures. The joint features highly localised stress and strain distributions due to its geometry, which themselves are representative of those found in large composite structural assemblies. Similarly, the thick layers of material selected in this joint are not typical of what would be seen in typical structural applications; however they were deemed necessary at this demonstration stage. This ensured that there were a sufficient number of image pixels across the thickness of each material layer to facilitate the DIC analysis. The DBSJ arrangement provides a significant measurement challenge that stretches the capability of the DIC approach. The symmetry of the joint reduces the eccentricity of the load path between adherends, which minimises the through-thickness stresses and strains that govern the joint failure. However, the adhesive spew filets, which reduce the severity of the discontinuity and the resultant stress concentrations [15] were removed during construction to increase the peel strains generated within the joint, to encourage failure.

## 3. Digital image correlation

Experimental analysis of the DBSJ was conducted using digital image correlation. This technique is becoming an increasingly popular analytical tool for structural mechanics applications due to the low price and availability of imaging equipment and correlation software. The theory behind DIC has been discussed in detail in literature, e.g. [20–23]. In brief, DIC is based on the comparison of white light images before, during and after the deformation of a test specimen. The images are divided into a grid of smaller interrogation cells, or subsets. The correlation between images is undertaken for each subset, creating a full-field array of displacement vector data points across the image. The spatial resolution and precision of the displacements calculated using DIC is limited by the number of pixels within the image and the size of the interrogation cells. In this study it is essential to have both high strain precision and high spatial resolution to analyse the load transfer occurring within the joint with confidence. However in the DIC processing parameters there is trade-off between spatial resolution and measurement accuracy due to limits in the number of pixels within the image and the size of the interrogation cells [24]. In the present research, the LaVision DaVis 7.4 correlation software is used, which employs a cross correlation algorithm using inverse fast fourier transforms. Subpixel displacement accuracy is obtained through the fitting of a two dimensional Gaussian parameter to the correlation function peak. Strains at each data point are evaluated numerically using the central difference method between the two adjacent deformation vectors in the x and y directions. This method can yield more noisy results, amplifying inaccuracies in the displacement field compared to least square fitting methods or finite element approaches. In order to compensate, large subset sizes (i.e. increasing the number of pixels in the subset) are used to increase the accuracy of the displacement field and minimise potential noise sources in the strain fields.

## 4. Equipment

Throughout the work described in this paper a 5MP 12 bit monochromatic LaVision E-lite camera was used. Nikon 50 mm, Sigma 105 mm and Canon MP-e65 macro lenses were used to capture images at three spatial resolutions of 30.8 pixels/mm, 250 pixels/mm and 726 pixels/mm respectively. At the lowest resolution, illumination was provided by a 72 W CREE XR-E Q3 LED floodlight. At the two higher resolutions a LED ring flash light was used to provide consistent cold lighting for the data collection. The DBSJ

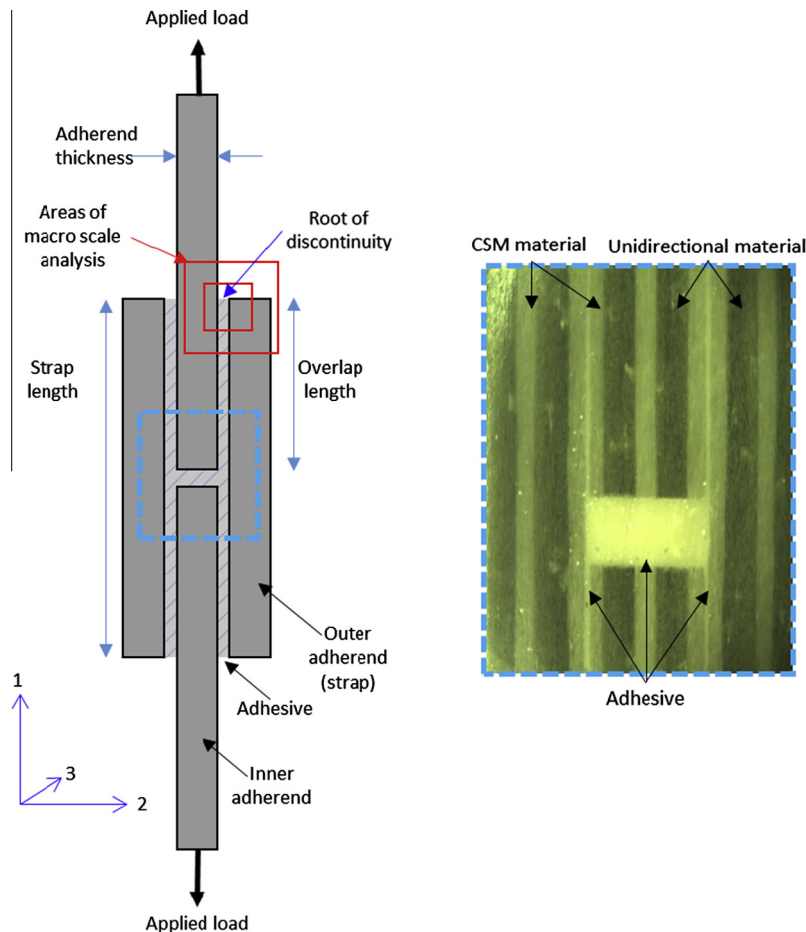


**Fig. 1.** Double butt strap joint (DBSJ), (a) schematic and (b) image of layered composite structure. (For interpretation of the references to colour in this figure legend, the reader is referred to the web version of this article.)

specimens were tested in an Instron 5569 electro mechanical test machine loaded at 2 mm/min up to failure.

The speckle patterns required for the DIC analysis were created using a high quality RS components matt black aerosol applied to a thin layer of matt white paint sprayed onto the specimen surface for the analysis at 30.8 and 250 pixels/mm. The optics used to image at the highest image magnification levels cause a significant change to the fundamental appearance of the speckle pattern. At this high magnification level, an airbrush with a 0.2 mm diameter nozzle was used to apply a black speckle pattern using Createx paint, matching the speckle size and pattern distribution to the image resolution. Evaluation of different pattern application methods has shown this approach provides the least measurement inaccuracy at high magnification; the work on the speckle evaluation approach is presented elsewhere [25].

## 5. Preliminary DBSJ analysis

An initial study was undertaken to investigate the strains in the material axis which develop within the joint up to failure. A stereo DIC configuration [20], using two cameras was used to measure the in-plane and out-of-plane displacements and the in-plane strains. Images were captured at 1 Hz during loading with an image spatial resolution of 30.8 pixels/mm. A schematic of the experimental set up is shown in Fig. 2. The specimen was viewed edge onto capture the through-thickness strains in the joint. The data was processed using a subset size of  $64 \times 64$  pixels and a subset overlap of 50% to

produce a spatial resolution of 1.04 mm between each processed strain data point, generating 22 data points across the 23 mm width of the joint.

Fig. 3a and b shows the axial and peel strains (denoted with axes 1 and 2) in the DBSJ specimen at 16 kN, which is 95% of the specimen failure load. Analysis of the loading sequence shows a widely uniform axial strain field throughout the joint. A high axial strain concentration is visible in the centre of the joint in Fig. 3a corresponding to the area of compliant adhesive at the butt between inner adherends. Two large peel strain concentrations can be identified at the discontinuity between the inner adherend and the outer strap in Fig. 3b, where the load path eccentricity between adherends is greatest. Analysis of the strain fields during loading shows that above 14.8 kN the peel strain concentration bisecting section A increases rapidly. A step change in horizontal displacements along section A through this high peel strain region at 14.8 kN is observed. This suggests that the recorded strain values are generated due to rigid displacement of the adherends caused by the growth of a crack, and not straining of the material. Clearly at this spatial resolution the location of the crack initiation and subsequent propagation cannot be accurately assessed, only providing a qualitative indication of the failure initiation site within the joint.

Images with greater spatial resolution are required to address the limitations in the analysis identified from the stereo DIC investigation. Greater spatial resolution, i.e. increasing the number of pixels per millimetre, can be achieved using a camera with a larger sensor array and hence increasing the number of interrogation

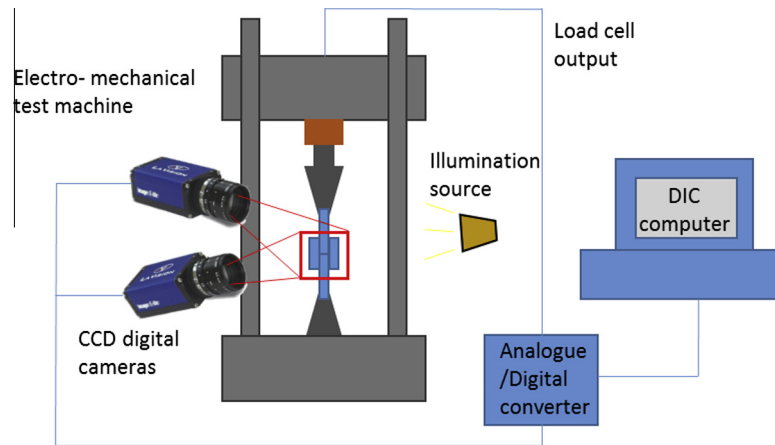


Fig. 2. Schematic of 3D DIC experimental set up. (For interpretation of the references to colour in this figure legend, the reader is referred to the web version of this article.)

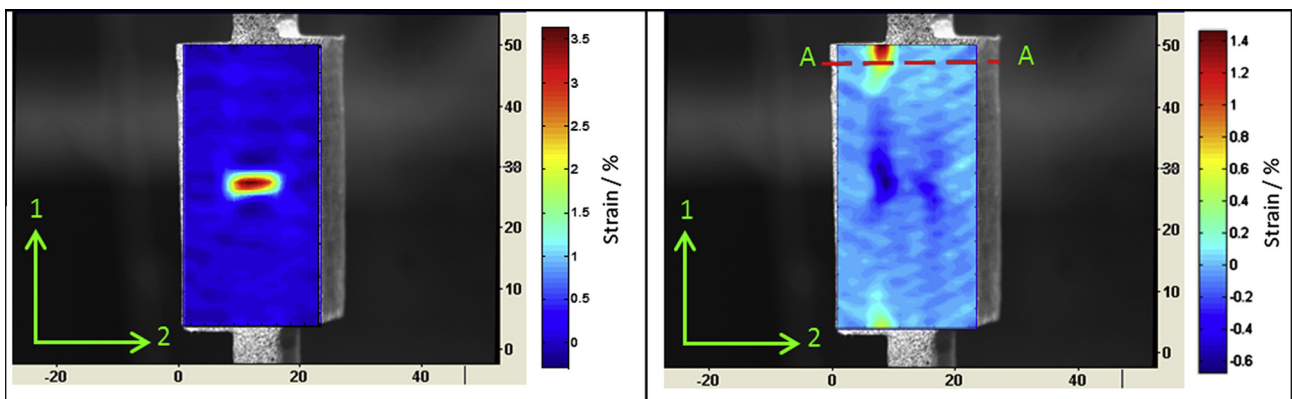


Fig. 3. Strain distribution in joint loaded at 16 kN, (a) axial ( $\epsilon_1$ ) and (b) through-thickness ( $\epsilon_2$ ). (For interpretation of the references to colour in this figure legend, the reader is referred to the web version of this article.)

cells within the analysis. These cameras however are expensive. An alternative approach is to use magnifying optics, providing an image with a high spatial resolution at the expense of reducing the size of the area of interest for analysis. Using this technique there is no need to compromise the size of the subsets in the analysis, as a large spatial resolution of data points/mm is obtained. This provides a high level of strain precision whilst retaining a high spatial resolution of data, both of which are essential for the accurate analysis of the joint.

Fig. 4 shows a detailed plot of the through-thickness strain distribution around the discontinuity in a DBSJ specimen loaded at 17 kN (80% of the specimen failure load) recorded using a 2D setup i.e. one camera aligned perpendicular to the joint face at 250 pixels/mm, delivering a spatial resolution of 7.8 data points per millimetre. A number of localised strain features can be identified in Fig. 4, showing the increase in magnification greatly improves the resolution and strain resolution compared with the initial global joint DIC analysis shown in Fig. 3. Strain concentrations are visible at the root of the discontinuity within the CSM layers in the inner and outer adherend, providing an indication of the local load path around the discontinuity, bisecting the high peel strain regions either side of the adhesive.

Although the level of detail in Fig. 4 is increased, this does not make the analysis of the strain fields more informative. The increased spatial resolution demonstrates that the behaviour at the root of the discontinuity in the adhesive joint is very heterogeneous, containing many localised strain features, which appear to exhibit some interdependency between adherends due to the

through-thickness loading around the discontinuity. The inhomogeneous nature of the CSM laminate structure, and the coupled nature of many of the key strain features, make precise analysis of the local load transfer and damage initiation mechanisms very difficult. Critically, at this spatial resolution there is still relatively poor quality to the DIC data. This is evident in the texture shown in the strain map which is caused by poor correlation due to the similarity between the pixel movement in the image associated with the camera CCD noise, and the pixel movement resulting from the small through-thickness deformation of the specimen under load. It is clear from the work described above that higher magnification is necessary to derive reliable strain values in the region of the discontinuity in the joint.

## 6. Meso scale strain field analysis

To address the errors and uncertainties in the strain measurements at 250 pixels/mm, the magnification of the images was increased using a high magnification macro lens. Increasing the magnification has the effect of increasing the observed pixel movement of the stochastic speckle pattern in the image for any given strain. As such when observing small deformations there is a large ratio between the speckle movement and sensor noise, giving more certainty to the correlated results.

An area of 3.1 mm  $\times$  2.6 mm was imaged at the root of the discontinuity with a spatial resolution of 769 pixels/mm; i.e. 25 times greater than the original global DIC joint analysis. Images

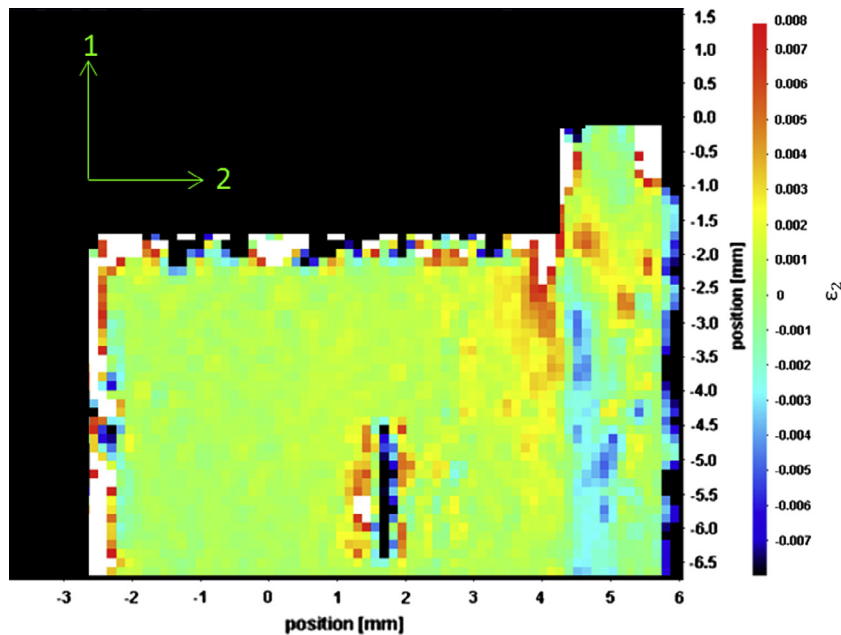


**Fig. 4.** Peel ( $\epsilon_2$ ) distribution in joint loaded at 17 kN under 250 pixels/mm. (For interpretation of the references to colour in this figure legend, the reader is referred to the web version of this article.)

were recorded at 0.5 kN intervals as the joint specimens were loaded to final failure. DIC was conducted using a  $128 \times 128$  pixel subset with 50% overlap. These are larger than previously used due to the increased movement of the specimen through the field of view at a given strain at the higher magnification; using smaller subsets made the displacement too large to correlate.

The short focal length and large dimensions of the macro lenses, required for the magnified imaging, limits analysis to a 2D system. The disadvantage of the 2D set up is that it is unable to determine out of plane movements, instead manifesting the motion as erroneous in-plane deformation. The earlier 3D DIC analysis had determined a maximum out-of-plane displacement of 0.2 mm. It was observed that this displacement occurred at the beginning of the testing when loading between 0 and 200 N, above which the out-of-plane displacement remained constant. This infers that the motion originates from settling of the machine grips under load, and not deformations from the loaded joint. Unfortunately this parasitic test machine compliance cannot be completely eliminated. An  $X$ - $Y$ - $\theta$  micro adjustable stage was used to finely adjust the alignment of the camera to ensure the camera was perpendicular to the specimen surface. A schematic of the test set-up is shown in Fig. 5.

At this high spatial resolution the 0.2 mm out-of plane-displacement generates an erroneous in-plane strain of approximately 0.8% which is very significant compared to the small strains being measured in the joint. At this resolution the depth of field is very narrow (below 0.2 mm), so out of plane displacement becomes very apparent during the test, prompting any tests experiencing significant out of plane displacements to be stopped and the test set-up recalibrated before retesting. It was found that by applying a small preload of 50 N to the specimen before testing, much of the parasitic out of plane displacement which resulted from the initial engagement and settling of the grips in the test machine was removed. This greatly improved the quality of the results and removes much of the concerns about out of plane displacement and erroneous in-plane measurement. A reduced loading rate of 1 mm/min was also used, as this was seen to minimise the effect of the parasitic movement of the grips and out-of-plane movement of the specimen as it is initially loaded.

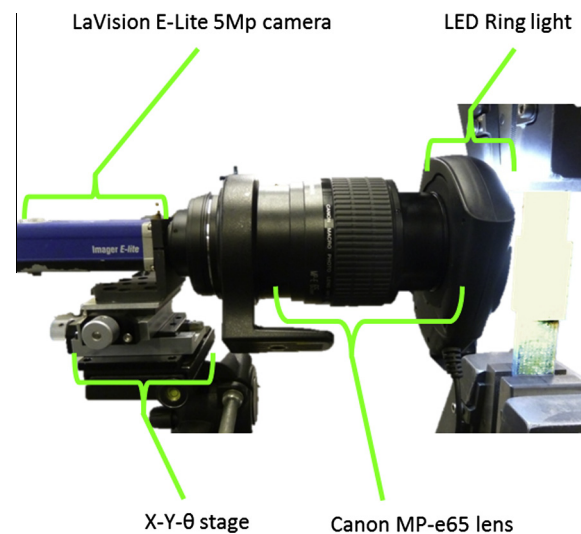


**Fig. 5.** High magnification DIC experimental set-up. (For interpretation of the references to colour in this figure legend, the reader is referred to the web version of this article.)

A brief test was conducted to establish the contribution of sensor noise on the DIC measurement at this high magnification level, and give confidence in the methodology. A sequence of 20 images were taken at 1 Hz using the experimental set up of a speckled DBSJ specimen mounted in the test machine with no load applied. The stationary images were processed in DaVis 7.4 using the correlation settings described above. The maximum measured deformation in both axes was 0.7 pixels, the maximum strains in the 1 and 2 directions were  $1.23 \times 10^{-3}\%$  and  $1.59 \times 10^{-3}\%$  respectively.

Fig. 6 shows full-field plots of the axial, peel, and shear strains in the principal material directions evaluated at 13 kN. An immediate improvement can be seen in the quality of the data in comparison to that shown in Fig. 5. At this magnification a spatial resolution of 24 data points per millimetre is achieved, allowing data rich analysis of the complex strain distributions observed

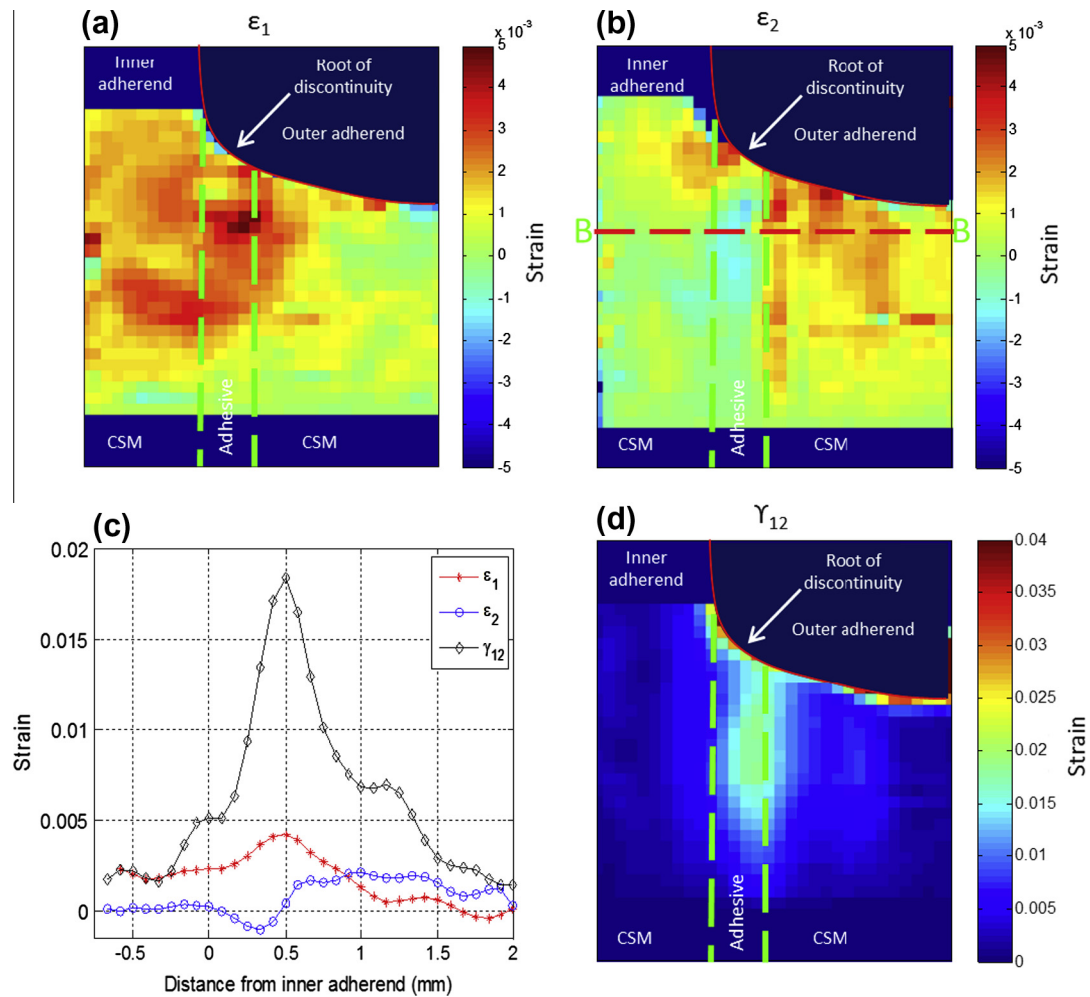


**Fig. 6.** Strain distributions around joint discontinuity at 13 kN, (a) axial ( $\epsilon_1$ ) strain field, (b) through-thickness ( $\epsilon_2$ ) strain field, (c) line plot of  $\epsilon_1$ ,  $\epsilon_2$ ,  $\gamma_{12}$  along section B and (d) shear strain ( $\gamma_{12}$ ). (For interpretation of the references to colour in this figure legend, the reader is referred to the web version of this article.)

within the joint. The axial strain plot in Fig. 6a shows considerable axial strain within the inner adherend. An axial strain gradient from within the inner adherend into the outer adherend can be observed, identifying load transfer across the adhesive layer. Two prominent peel strain concentrations are identified in Fig. 6b, peaking at 0.3% strain either side of the root of the discontinuity. The first peel strain concentration is located at the root of the discontinuity in the inner adherend, adjacent to the interface with the adhesive layer. The second strain concentration forms in the outer adherend adjacent to the root of the discontinuity. This location identifies a substantial through-thickness deformation of the outer adherend due to the eccentricity of the load path around the geometric discontinuity between adherends. Fig. 6c shows a line plot of the axial, peel and shear strains 0.25 mm below the root of the discontinuity indicated by the red broken line B-B in Fig. 6b. Fig. 6c identifies the load transfer across the 0.6 mm thick adhesive layer, showing a large increase in peel strain between the inner and outer adherends, with the strain in the outer adherend over four times greater than that in the inner adherend. A region of compression can also be observed within the adhesive as the outer strap peels away and compresses the bondline as it rotates. There is a corresponding reduction in axial strain across the adhesive in the outer adherend due to the presence of the zero stress boundary condition at the free edge.

The shear strain distributions shown in Fig. 6c and d show high shear strains isolated within the compliant adhesive layer between

adherends. The shear strain peaks just below the root of the discontinuity, showing a decrease in strain towards the unloaded horizontal free edge of the outer adherend. This shear strain distribution is not uniform across the thickness of the bond layer. Fig. 6b and d both shows the location of the maximum shear strains correspond with the location of the greatest peel strains at the interface with the outer adherend. This indicates a strong interaction between the adhesive layer and outer adherend due to load transfer between the inner and outer adherends in the through-thickness direction. Therefore, the behaviour at this highly loaded interface area between the compliant adhesive and the relatively stiff CSM material in the outer adherend, is seen as critical in the control and initiation of damage.

The strain distributions show good agreement to the results in literature observed by Haghani et al. [13] and Ruiz et al. [16]. This gives confidence in the experimental methodology, showing that the observed strains are representative of typical joint structural behaviour, and not an observation resulting from the highly heterogeneous fibre/matrix bundles of the CSM material.

Damage is observed to occur in Fig. 7 when the specimen is loaded to 17 kN. Noticeably there is a large reduction in the axial strain in the outer adherend, shown in Fig. 7a. This discontinuity in the axial strain field indicates that load is no longer being transferred between adherends across the damaged region, and is therefore an indication of failure in the joint structure as opposed to local damage of the speckle pattern coating. The peel and shear

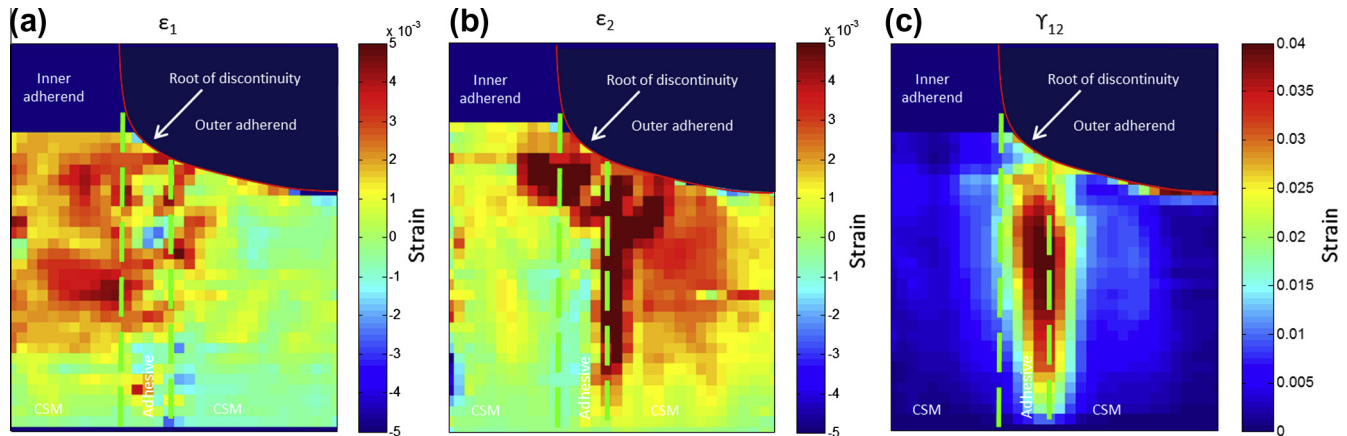


**Fig. 7.** Strain distributions around joint discontinuity at 17 kN, (a) axial ( $\epsilon_1$ ), (b) through-thickness ( $\epsilon_2$ ) and (c) shear strain ( $\gamma_{12}$ ). (For interpretation of the references to colour in this figure legend, the reader is referred to the web version of this article.)

strains at the interface area between the adhesive and outer adherend also become very large at this load, shown in Fig. 7b and c. These large strains are produced as a result of rigid body displacement of the adherend due to the presence of damage at this interface. This damaged interface provides a preferential route for damage to propagate. However, the final failure of the joint initiates from the small localised peel strain concentration at the root of the discontinuity in the inner adherend identified in Fig. 6b. A crack propagates quickly along the interface between the inner adherend and the adhesive, resulting in light fibre-tear failure as categorised by ASTM D5573.

## 7. Evaluation of material properties for stress analysis

Figs. 6 and 7 provide a quantitative analysis of the strain fields generated around the root of the discontinuity within the joint. However from this analysis it is not possible to directly relate the strains to the development of damage in the joint. To provide full analysis of the load transfer and damage mechanisms, it is necessary to derive the stresses in the composite structure.

The stresses in the principal material directions (i.e. the 1 and 2 directions) can be obtained from strains derived from the DIC presented in Figs. 6 and 7, and the material stiffness matrix,  $[Q]_{12}$ , using the following relationship [4]

$$\begin{bmatrix} \sigma_1 \\ \sigma_2 \\ \tau_{12} \end{bmatrix} = [Q]_{12} \begin{bmatrix} \epsilon_1 \\ \epsilon_2 \\ \gamma_{12} \end{bmatrix} \quad (1)$$

The material stiffness matrix was obtained from the experimentally established constitutive material properties shown in Table 1 along with the coefficients of variation from the experimental tests.

The Young's modulus in the axial direction, i.e.  $E_1$ , for the CSM material was obtained from six ASTM D3039 tensile specimens loaded at 2 mm/min in an Instron 5569 test machine. Coupon specimens were manufactured from 4 layers of 450 g/m<sup>2</sup> CSM material, using Gurit Prime 20LV epoxy resin and the resin infusion method, in a similar manner to that used to manufacture the joints. The axial strain was recorded using an Instron 2630-113 clip gauge extensometer with a 50 mm gauge length.

**Table 1**  
Materials properties values for CSM and Araldite 2015 materials.

Material	$E_1$ (GPa)	$E_2$ (GPa)	$\nu_{12}$	$\nu_{21}$	$G_{12}$ (GPa)
CSM	11.27	7.63	0.344	0.233	2.484
	6.43%	7.43%	3.43%		17.7%
Araldite 2015	2 [26]	2 [26]	0.36 [17]	0.36 [17]	0.9 [26]

The through-thickness modulus of the CSM material,  $E_2$ , was evaluated from high aspect ratio through-thickness laminate specimens, in an experimental procedure very similar to that used by Boyd et al. [18] in the evaluation of the through-thickness thermoelastic properties of composite materials. High aspect ratio through-thickness specimens with a target ratio of 2.5 were manufactured by bonding 10 mm thick 30 mm × 30 mm laminate sections of CSM laminate together between a 25 mm × 25 mm × 25 mm aluminium end tab fitting using Araldite 2015. The overlap between the laminate and the aluminium end tabs were machined flush with the grips to ensure flat, adhesive free measurement surfaces.

The material properties were established from the surface strains measured using DIC. Painted speckle patterns with a white background and black speckles were applied, before being placed in an Instron 5569 mechanical test machine and loaded at 2 mm/min up to 4 MPa. Images were recorded during the loading sequence using a LaVision E-lite 5 Mp camera imaged at 59 pixels/mm resolution. 2D DIC was conducted using the LaVision Davis 7.4 correlation software to analyse the strain distribution present in the specimens using a subset size of 128 × 128 pixels with an overlap of 50%.

The through-thickness Poisson's ratio  $\nu_{12}$  for the CSM material was obtained from testing of modified, 8 mm thick, ASTM D3039 coupons manufactured with 16 layers of CSM material. A Tokyo Sokki Kenkyujo Co FCA-3-32 biaxial strain gauge was bonded onto the edge of each thick specimen to measure the in-plane and through thickness strains. Manipulation of the experimentally obtained  $E_1$ ,  $E_2$  and  $\nu_{12}$  values was used to evaluate the  $\nu_{12}$  Poisson's ratio.

The shear modulus,  $G_{12}$ , was obtained from analysis of six shear specimens constructed from 8 mm thick CSM laminate coupons measuring 40 mm × 40 mm bonded between two steel shear plates using Araldite 2015. The specimens were fixed to an Instron 5569 test machine using a threaded tie rod with a universal end joint, such that the line of action of the load passed through opposing corners of the specimen, loading the specimen in pure shear. The specimen shear strains were recorded using 2D DIC analysis with a spatial resolution of 38 pixels/mm and subset size of 79 × 79 pixels in DaVis 8.0. The coefficient of variation between these six specimens is relatively high due to the random orientation of fibres in the CSM material.

Material properties for the Araldite adhesive are taken from the manufacturers data sheet [26]

## 8. Deriving stresses from the strain data

A Gaussian filter, with a kernel size of 3 × 3 data points and a standard deviation of 1.5, was applied to the DIC strain field data

of the joint. This was done to minimise residual noise in the data, which causes difficulty in the subsequent manipulation into principal stresses using Mohr's circle, discussed below. Filtering reduces the fluctuations in the data, ensuring better continuity between the strain fields. These fluctuations can be large and highly detrimental due to the large magnitude of the shear stress relative to the axial and peel components. The small kernel size was chosen to minimise the loss of localised strain concentrations across the thin adhesive layer between adherends. Using a larger kernel size would result in filtering the peak values at the interface. Fig. 8 shows the stresses in the principal material directions derived from the strain data given in Fig. 6 and the material properties given in Table 1 using Eq. (1). The stress distributions closely match the strain fields observed in Fig. 6. The main difference is identified in the adhesive layer, where due to the compliant material properties of the Araldite 2015 adhesive, the stresses are low, as is shown in the line plot across the joint in Fig. 8c. The shear modulus of the CSM material which interfaces with the adhesive is over 2.5 times greater than that of the adhesive, and as a result, large interfacial shear stresses are observed within the composite adherends.

Analysis of the stresses in the principal material directions at 16 kN, i.e. prior to damage occurring at 17 kN, shows the maximum axial, peel and shear stresses within the damage initiation region to be 70 MPa, 45 MPa and 77 MPa respectively. This results in a

significant mixed-mode loading at the interface. It is very difficult therefore to succinctly evaluate the individual influence on each of these stresses towards the initiation of damage. It is the principal stresses which govern failure in the brittle matrix leading to inter-laminar crack which promotes damage propagation. Therefore, when assessing the damage development and initiation within the joint it is important to consider the principal stresses and not the stresses in the principal material directions.

The principal stresses,  $\sigma_1^p$ ,  $\sigma_2^p$ , are obtained using a simple Mohr's circle analysis. It is important to note that due to the discontinuous nature of the joint geometry the principal stress direction is different at every location around the discontinuity. Therefore the Mohr's circle transformation of stresses was conducted on a point by point basis. Fig. 9 shows plots of the principal stresses and maximum shear stress derived from the data given in Fig. 8. The very high maximum principal stress in the interface region where the damage initiates is clearly identified in Fig. 9a. The average maximum principal stresses at the interface is 60 MPa, increasing to about 80 MPa closer to the discontinuity.

The discontinuity between the adherends, and high shear strains around the adhesive, result in a rotation of the principal stress direction of between 35° and 45° from the vertical. This means that the maximum principal stresses are approximately one and a half times that of the peak axial stress shown in

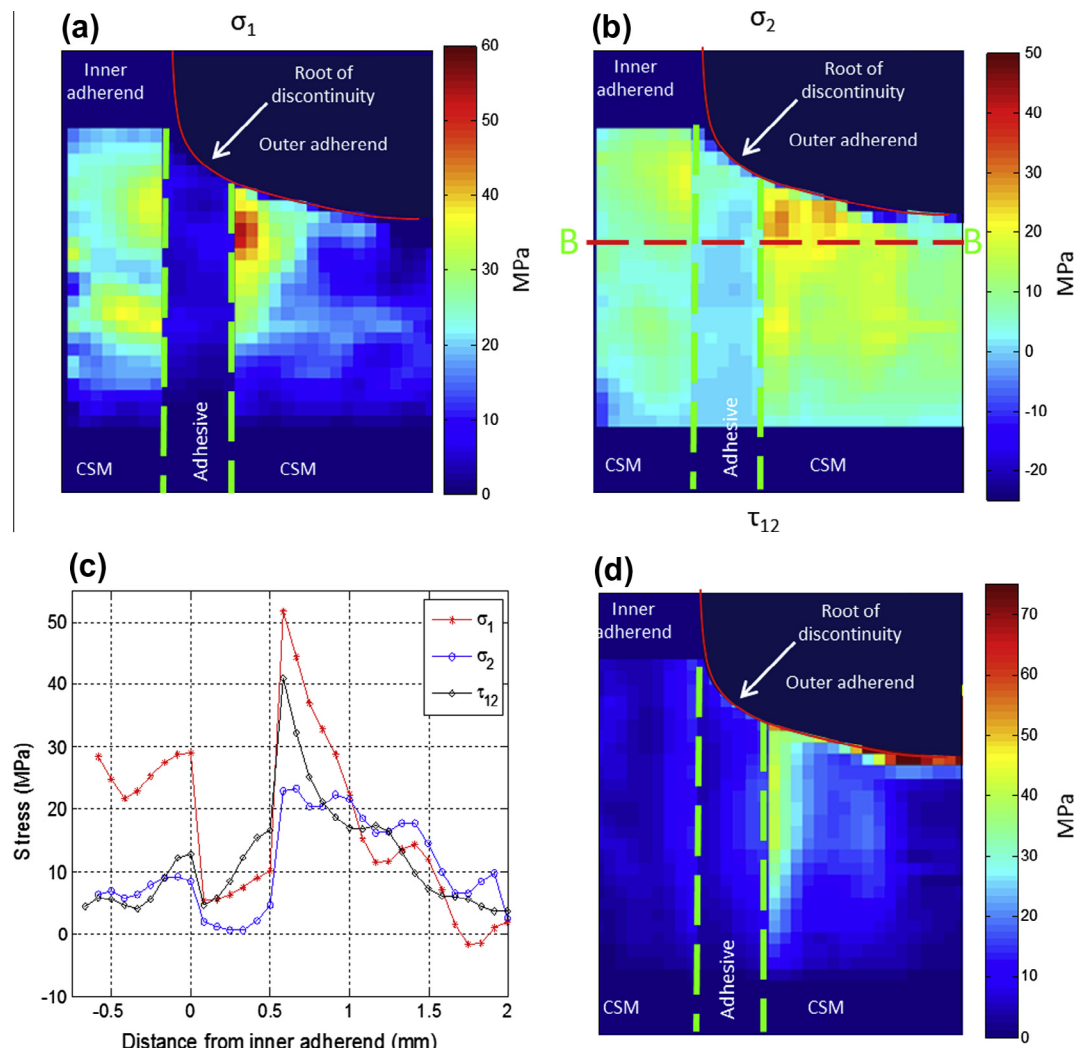


**Fig. 8.** Strain distributions around joint discontinuity at 13 kN. (a) axial ( $\sigma_1$ ), (b) through-thickness ( $\sigma_2$ ), (c) line plot of  $\sigma_1$ ,  $\sigma_2$ ,  $\tau_{12}$  along section B and (d) shear stress ( $\tau_{12}$ ). (For interpretation of the references to colour in this figure legend, the reader is referred to the web version of this article.)

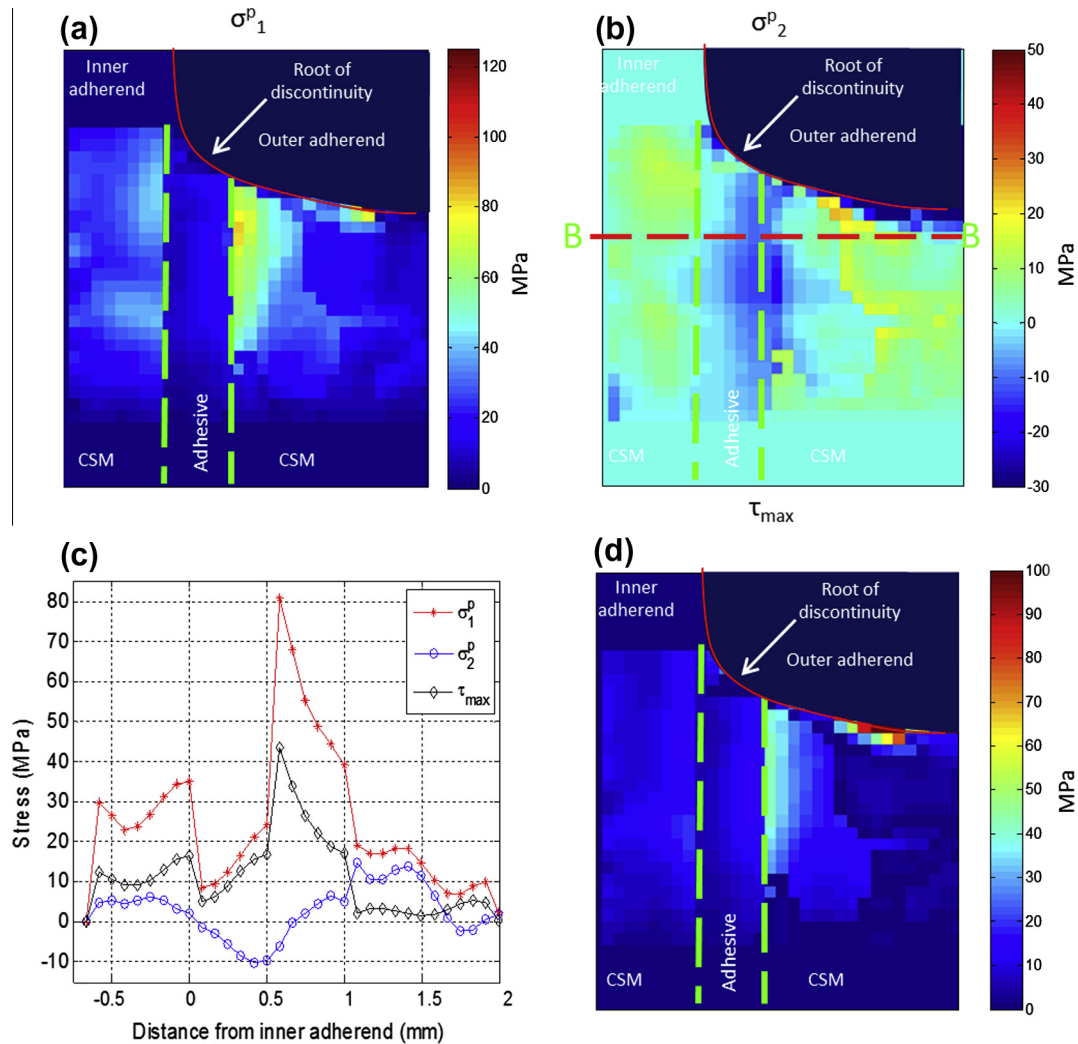


**Fig. 9.** Principal stress distributions at 13 kN, (a) maximum principal stress ( $\sigma_1^p$ ), (b) minimum principal stress ( $\sigma_2^p$ ), (c) line plot of  $\sigma_1^p$ ,  $\sigma_2^p$ ,  $\tau_{\max}$  along section B and (d) maximum shear stress ( $\tau_{\max}$ ). (For interpretation of the references to colour in this figure legend, the reader is referred to the web version of this article.)

**Fig. 8a.** Minimum principal stresses of  $-20$  MPa are shown in **Fig. 9b** along the adhesive interfaces in the inner and outer adherends. The maximum shear stresses are located in the relatively stiff CSM material at the adhesive interface with the outer strap, corresponding to the high shear strain areas identified in **Fig. 6d**.

As the load increases up to 15 kN the maximum principal stresses in **Fig. 10a** remain concentrated along the adhesive interface with the outer adherend, increasing up to 115 MPa at the root of the discontinuity. Stresses within the inner adherend show little increase in stress at this higher load level, showing the stress concentrating effect of the geometric discontinuity to have greatest effect in the outer adherend. The line plot in **Fig. 9c** again clearly shows the localisation of the stresses at the material interfaces.

At 16 kN there is a large change in the shape and magnitude of the maximum principal stress concentration as shown in **Fig. 11a**. A maximum change in stress of 50 MPa is observed, reaching a maximum of 150 MPa along the interface region. This high stress region is very localised, with a large stress gradient to the surrounding stress values at the interface. The sharp isolated change in the stresses suggests that they are a result of localised damage in the material, and are not representative of the intact material response. A similar breakdown in the continuity of the analysis can also be seen in the analysis of the minimum principal and maximum shear fields.

**Fig. 11b** shows a magnified view of the raw image within the highlighted area in **Fig. 11a** used to conduct the DIC. Three very

small thin cracks are visible along the interface with the outer adherend in the region where the very high maximum principal stress was recorded. These very small cracks were overlooked in the strain analysis as the axial strain field had shown the load transfer between the inner and outer adherends to still be intact, suggesting load transfer through fibre bridging across the damage. The high interfacial peel and shear strains recorded in this region also masked the significance of the strain changes in this area due to the small size of the cracks. **Fig. 11b** shows these cracks are aligned close to  $45^\circ$  clockwise from the vertical. Analysis of the principal stress direction at 15 kN in the undamaged joint condition shown in **Fig. 11c** show good agreement between the principal stress and crack directions, indicating failure due to a mainly mode 1 opening of the crack in the adhesive at the adhesive interface.

Unfortunately there is insufficient temporal resolution to capture the initiation of failure in the inner adherend, though it is strongly suspected from all of the stress and strain field analyses undertaken that the localised damage at the outer adherend interface provides relief of the stresses concentrated in the outer adherend. Unable to transfer load across the damaged region to the outer adherend, the root of the discontinuity in the inner adherend quickly becomes highly stressed, and interlaminar cracking of the CSM laminate occurs in the region of the peel stress concentration observed in **Fig. 9b**.

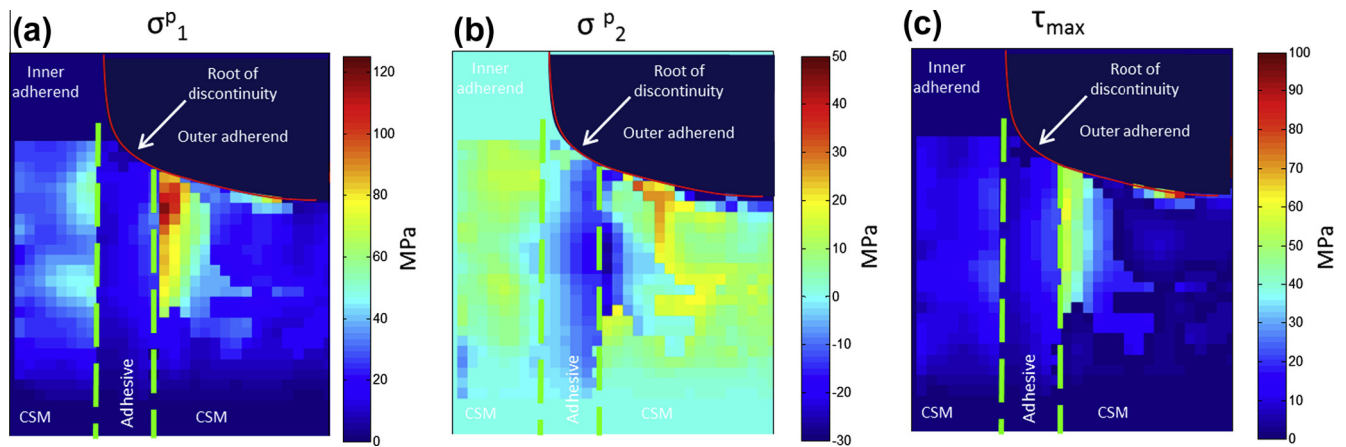


**Fig. 10.** Principal stress distributions at 15 kN, (a) maximum principal stress ( $\sigma_1^p$ ), (b) minimum principal stress ( $\sigma_2^p$ ) and (c) maximum shear stress ( $\tau_{max}$ ). (For interpretation of the references to colour in this figure legend, the reader is referred to the web version of this article.)

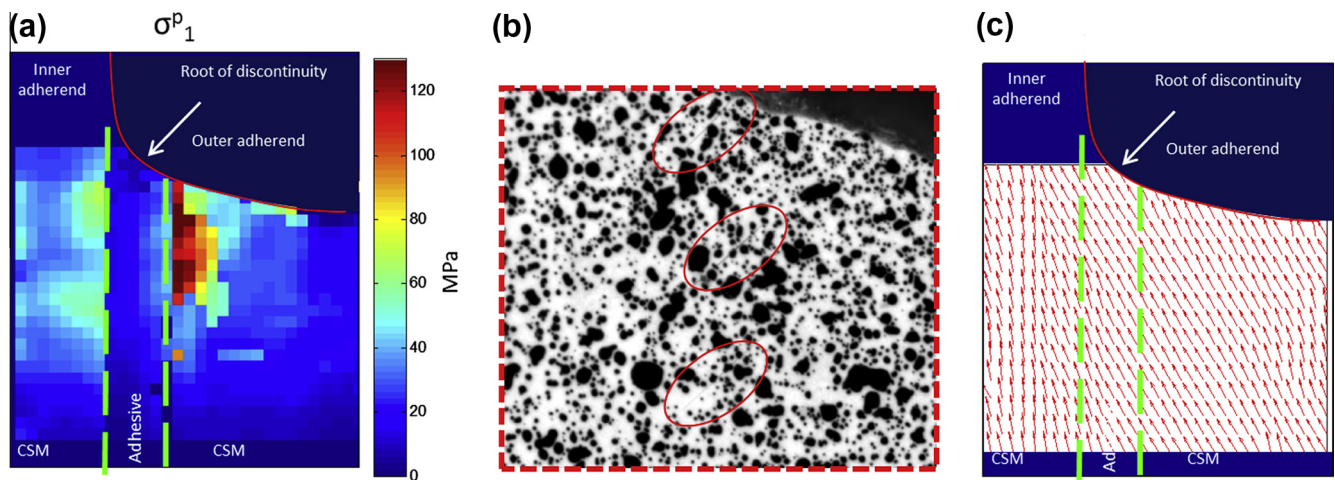


**Fig. 11.** Joint behaviour, (a) maximum principal stress ( $\sigma_1^p$ ) at 16 kN, (b) raw image of joint at 16 kN and (c) maximum principal stress direction at 15 kN. (For interpretation of the references to colour in this figure legend, the reader is referred to the web version of this article.)

Analysis of the principal stresses delivers a comprehensive evaluation of the development of damage within the joint. The stress fields compliment the strain analysis and provide clear analysis of the load transfer and damage initiation process within the joints. Using analysis of the principal stresses, the location of damage initiation becomes very clear. Importantly, damage is identified 1 kN earlier than from analysis of the principal material strains, providing a clearer understanding of the critical stresses in the initiation of damage, and the subsequent behaviour of the joint as it fails. The maximum failure stress criteria is shown to be a much more effective damage assessment criteria for the analysis of the composite bonded assembly, due to the large mixed-mode loading within the component between adherends. Damage critical behaviour is observed above a maximum principal stress value of 115 MPa within the joint. Only through analysis of the principal stresses were the very small, yet highly critical, interfacial cracks in the outer adherend identified. Analysis of the stress or strain fields in the principal material directions does not provide this information. A validation study has been carried out and is summarised in [27]. The validation was based on independent full field data derived from TSA; a detailed account of the steps to make the DIC and TSA data comparable is the subject of a future publication.

Additionally the authors have studied more simple single lap joints in this material [28] which have demonstrated very good agreement with analytical models and experimental results in the literature [29,15].

## 9. Conclusions

Component strains within a composite DBSJ are evaluated over three increasing magnification levels using DIC, revealing complex localised strain distributions present around the geometric discontinuity between adherends. High resolution strain data of very small, yet critical, localised through-thickness and shear strains evolving within the joint up to failure were generated at the highest magnification level with a high degree of confidence. The full-field results show good agreement with previous experimental investigations in literature, validating the experimental macro 2D DIC methodology discussed in this paper. Peel strain concentrations were observed at the root of the discontinuity in the inner adherend and at the interface between the adhesive layer and the outer adherend. Shear strains were observed to be non-uniform through the thickness of the adhesive, concentrating at the adhesive interface with the outer adherend, where high peel

strains are also recorded. Analysis of the strain fields within the joint is used to evaluate the load transfer between adherends, and investigate the role of the strain components on the initiation of damage within the joint. The interfacial strain concentrations exhibit a coupled response indicating significant load transfer across this interface, and generate a critical high strain region for the initiation of damage, although the major damage development was identified at the root of the discontinuity in the inner adherend.

The full field strain data was manipulated to provide analysis of the accompanying stress states in the principal material, and principal stress directions around the discontinuity of the joint. Analysis of the stresses in the principal stress direction, which govern failure in the brittle matrix material, provide a full evaluation of the stresses within the joint responsible for damage and failure. Presentation of the stresses in the principal material directions within the joint concisely identifies the first occurrence of damage within the joint at the interface between the outer adherend and the adhesive layer. A greater understanding of the material behaviour within the highly complex stress and strain fields generated around the geometric discontinuity was obtained through this analysis. This result demonstrates the importance of evaluating both the stress and strain distributions within complex structures when using full-field data to obtain accurate knowledge of the structural response.

## References

- [1] Pocius A. Adhesion and adhesives technology: an introduction. 2nd ed. Hanser Publications; 2002.
- [2] da Silva LFM, Öchsner A, Adams RD. Handbook of adhesion technology. Berlin, Heidelberg: Springer; 2011.
- [3] Banea MD, da Silva LFM. Adhesively bonded joints in composite materials: an overview. Proceedings of the Institution of Mechanical Engineers, Part L: Journal of Materials: Design and Applications Jan. 2009;223(1):1–18.
- [4] Daniel I, Ishai O. Engineering mechanics of composite materials. Oxford University Press; 2005.
- [5] da Silva L, Adams RD. Techniques to reduce the peel stresses in adhesive joints with composites. Int J Adhesion Adhesives 2007;27(3):227–35.
- [6] Keller T, Vallée T. Adhesively bonded lap joints from pultruded GFRP profiles. Part II: joint strength prediction. Compos Part B: Eng 2005;36(4):341–50.
- [7] Kaye RH, Heller M. Through-thickness shape optimisation of bonded repairs and lap-joints. J Adhesion 2002;22:7–21.
- [8] Lang TP, Mallick PK. Effect of spew geometry on stresses in single lap adhesive joints. J Adhesion 1998;18:167–77.
- [9] Raos P, Kozak D, Lucic M. Stress strain analysis of single lap tensile loaded adhesive joints, In: Proceedings of the 9th International Conference on Numerical Methods in Industrial Forming Processes. p. 1093–98.
- [10] Wang ZY, Wang L, Guo W, Deng H, Tong JW, Aymerich F. An investigation on strain/stress distribution around the overlap end of laminated composite single-lap joints. Compos Struct 2009;89(4):589–95.
- [11] Colavito KW, Gorman J, Madenci E. Refinements in digital image correlation technique to extract adhesive strains in lap joints. In: Proc 50th AIAA/ASME/ASCE/AHS/ASC structures, structural dynamics, and materials conference; 2009. p. 5031.
- [12] M. D. Colavito E.M.K, Hahs D. Digital image correlation for adhesive strains in bonded composite lap joints. In: 49th AIAA/ASME/ASCE/AHS/ASC structures, structural dynamics, and materials conference; 2008. p. 2008–2008.
- [13] Haghani R, Al-Emrani M, Kliger R. Effects of geometrical modifications on behaviour of adhesive joints used to bond CFRP laminates to steel members – experimental investigation. In: Proc Nordic steel construction conference; 2009.
- [14] Moutrille M-P, Derrien K, Baptiste D, Balandraud X, Grédiac M. Through-thickness strain field measurement in a composite/aluminium adhesive joint. Compos Part A: Appl Sci Manuf 2009;40(8):985–96.
- [15] Tsai MY, Morton J, Matthews FL. Experimental and numerical studies of a laminated composite single-lap adhesive joint. J Compos Mater 1995;29(9):1254–75.
- [16] Ruiz PD, Jumbo F, Huntley JM, Ashcroft IA, Swallowe GM. Experimental and numerical investigation of strain distributions within the adhesive layer in bonded joints. Strain 2011;47(1):88–104.
- [17] Boyd SW, Dulieu-Barton JM, Thomsen OT, Gherardi A. Development of a finite element model for analysis of pultruded structures using thermoelastic data. Compos Part A: Appl Sci Manuf 2008;39(8):1311–21.
- [18] Boyd SW, Dulieu-Barton JM, Thomsen OT, El-Gazzani S. Through thickness stress distributions in pultruded GRP materials. Compos Struct 2010;92(3):662–8.
- [19] Rastogi P, Hack E. Optical methods for solid mechanics. Wiley; 2012.
- [20] Sutton MA, Orteu J-J, Schreier HW. Image correlation for shape, motion and deformation measurements: basic concepts, theory and applications. Springer; 2009.
- [21] Pan B. Recent progress in digital image correlation. Exp Mech 2011;51:1223–35.
- [22] Pan B, Qian K, Xie H, Asundi A. Two-dimensional digital image correlation for in-plane displacement and strain measurement: a review. Measur Sci Technol 2009;20(6):062001.
- [23] Hild F, Roux S. Digital image correlation: from displacement measurement to identification of elastic properties – a review. Strain 2006;42(2):69–80.
- [24] Triconnet K, Derrien K, Hild F, Baptiste D. Parameter choice for optimized digital image correlation. Opt Lasers Eng 2009;47(6):728–37.
- [25] Crammond G, Boyd SW, Dulieu-Barton JM. Speckle pattern quality assessment for digital image correlation. Opt Lasers Eng 2013;51(12):1368–78.
- [26] Huntsman, Araldite 2015 Data Sheet; 2007. [Online]. Available: <<http://www.intertronics.co.uk/data/ara2015.pdf>>.
- [27] Crammond G, Boyd SW, Dulieu-Barton JM. A validated point-wise approach to the analysis of complex composite structures using digital image correlation and thermoelastic stress analysis. In: Proceedings of PhotoMechanics 2013 – International conference on full-field measurement techniques and their applications in experimental solid mechanics. Montpellier, France, p. 15–8.
- [28] Crammond G, Boyd S, Dulieu-Barton J. Dynamic analysis of composite marine structures using full-field measurement. J Mar Eng Technol. ACCEPTED SUBJECT TO MINOR CORRECTIONS; 2014.
- [29] Goland M, Reissner E. The stresses in cemented joints. J Appl Mech 1944;11:17–27.